16th World Conference on Earthquake Engineering, 16WCEE 2017
Santiago Chile, January 9th to 13th 2017
Paper N° 1568 (Abstract ID)
Registration Code: S-C1464609106

Seismic Response Analysis of an Interacting Train-Bridge System considering Derailment

Qing. Zeng[(1)], Elias G. Dimitrakopoulos[(2)]

[(1)] *PhD Candidate, Department of Civil and Environmental Engineering, Hong Kong University of Science and Technology, Clear Water Bay, Kowloon, Hong Kong, qzeng@ust.hk*

[(2)] *Assistant Professor, Department of Civil and Environmental Engineering, Hong Kong University of Science and Technology, Clear Water Bay, Kowloon, Hong Kong, ilias@ust.hk*

Abstract

This paper investigates the seismic behavior of an interacting train-bridge system. The study models the three dimensional vehicle as a multibody assembly. Each component of the vehicle is a rigid body connected with springs and dashpots, representing the suspension system. The bridge is simulated using the finite element method. The practical nonlinear profiles of both the wheels and the rails are taken into account. The wheel-rail contact along the normal direction follows the principles of non-smooth mechanics. The calculation of tangential contact forces, including the lateral creep force, the longitudinal creep force and the pin moment, is based on the nonlinear creep theory. When the relative lateral displacement between the wheel and the rail exceeds the clearance under earthquakes, flange contact takes place. Based on the proposed interaction model, the scheme investigates the effect of the seismic induced vibration of the bridge to the safety of the train operation, especially the derailment of the wheel off the rail during earthquakes. If simulated properly, the multibody vehicle acts as a damper to the bridge system and reduces the pertinent response of the bridge. On the contrary, conventional seismic code seismic analysis of bridges considers trains as merely additional mass on the bridge and overestimates the response of the bridge. The results underline the importance of a realistic train-bridge-interaction during seismic response. The seismic induced vibration of the bridge has a significant adverse effect on the response of the vehicle above. The proposed contact model can capture the wheel-rail flange contact, the detachment, the uplifting and the recontact phenomena, under strong earthquakes.

Keywords: train-bridge interaction; seismic response; non-smooth dynamics; derailment; wheel-rail separation

1. Introduction

High speed railway (HSR) lines extend for thousands of kilometers within earthquake prone areas. Bridges may constitute even more than 80% of the total length of a HSR line [1]. As a consequence, the possibility that a train is running on a bridge during earthquake shaking is far greater than otherwise. In the short history of HSR, trains have already derailed on bridges shaken by earthquakes. Two alarming accidents (Fig. 1) were already reported in the last 15 years. On 23 October 2004 in Japan, during the Niigata Chuetsu earthquake (magnitude 6.8), a Shinkansen train (200 km/h) derailed, just 9.8 km from the epicenter (Fig. 1 (b)) [2]. The driver felt the earthquake and applied the brakes manually, as the epicenter was too close for the automatic braking system to be activated [2]. The train derailed on a viaduct and came to full stop after 1.5 km [2]. On 04 March 2010 in Taiwan during the Jiashian earthquake (magnitude 6.4), a HSR train running at 298 km/h derailed, 53 km away from the epicenter (Fig. 1 (a)). The peak ground acceleration (PGA) amplitudes at the location of the derailment were only low to moderate: 95 cm/s^2 along the direction of the railway, 171 cm/s^2 perpendicular to the rails and 37 cm/s^2 in the vertical direction, respectively [3]. The disaster warning system activated the brake system 1.87 s after the detection of the earthquake, but it took 76 second (s) and 3.3 km for the train to come to a full stop [3].

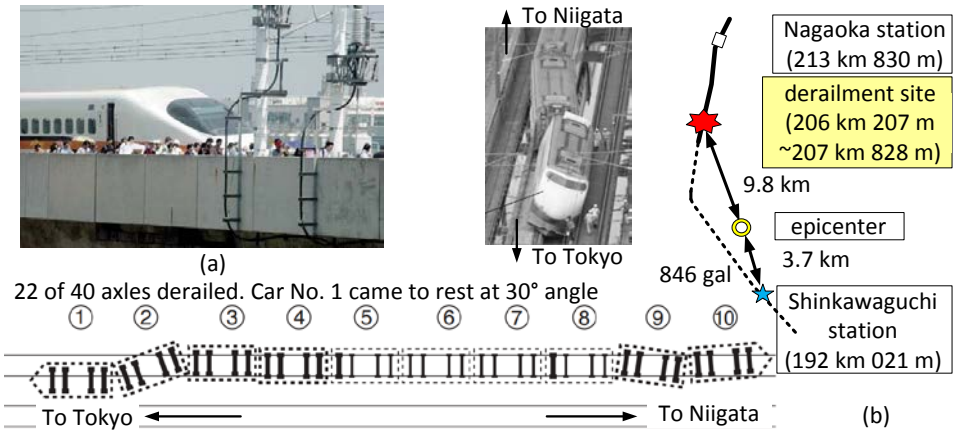

Fig. 1 – Derailment of high-speed trains on bridges due to earthquakes: (a) Jiashian earthquake in Taiwan [4]; (b) Niigata Chuetsu earthquake in Japan [2].

Most seismic vehicle-bridge interaction (SVBI) studies originate from Japan, China or Taiwan, and examine the safety of trains running over bridges during earthquakes. More specifically, Yang and Wu [5] studied the stability of 3D trains, stationary or travelling, over bridges shaken by earthquakes. That SVBI analysis used four historic earthquake records, normalized to a moderate intensity of 0.08g PGA. The results concluded that under the ground motions examined, a train on a bridge was safer when stationary and stressed the influence of the vertical component of ground motion on the stability of the vehicle. A study by Tanabe et al. [6] attempted to simulate the interaction between the wheel and the rail in both the pre-derailment state and the post-derailment state, under an earthquake. Ju [7] investigated the danger of derailment of high-speed trains

moving on multi-span simply supported bridges during earthquakes with the *derailment factor*. Based on the Hertz normal contact model, Du et al. [8] took into account the possible separations and recontact between the wheel and the rail with the Hertz normal contact thoery, under non-uniform seismic ground motions. That study concluded that the probability and the duration of wheel-rail detachment increased with train speed. Very recently, Montenegro et al. [9] proposed a refined nonlinear wheel-rail contact simulation suitable also for seismic analyses. The model was verified with experimental data on a rolling stock plant simulating track deviations caused by earthquakes. The vast majority of SVBI investigates the danger of derailment with pertinent metrics, e.g. the *derailment factor* and the *offload factor*, and do not model the wheel-rail separation. The present study is motivated by the need to capture the flange contact, the detachment, the uplifting and the recontact phenomena between the wheel and the rail directly.

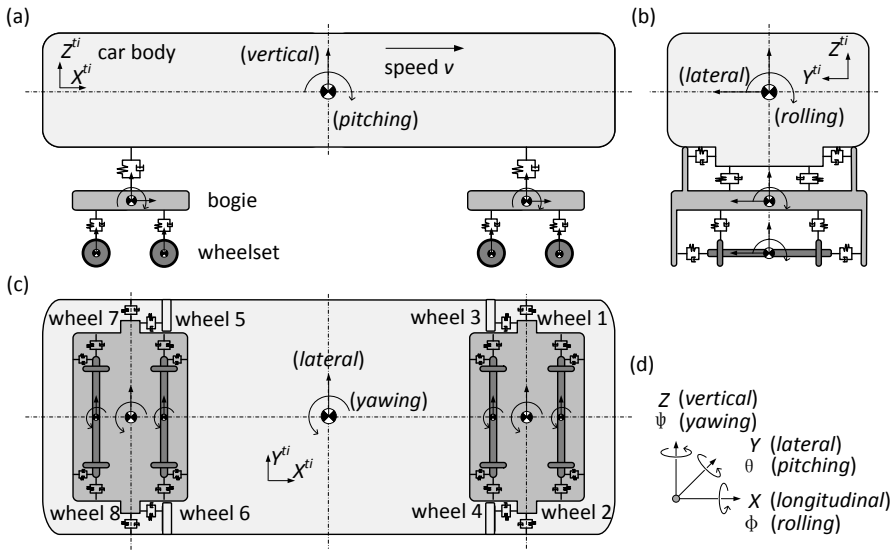

Fig. 2 – The degrees of freedom (DOFs) of the vehicle system: (a) side view, (b) top view, (c) back view.

2. Vehicle modelling

The study simulates each train vehicle as a multi rigid-body assembly as in [1, 10, 11]. Fig. 2 presents a typical three dimensional (3D), four-axle vehicle model. Each vehicle consists of one car body, two bogies and four wheelsets. All the components, i.e. the car body, bogies and wheelsets are considered as rigid bodies, neglecting their elastic deformations. They are connected with springs and dashpots, representing the properties of the suspension systems. The train consists of a series of (usually identical) vehicles and it travels with a constant speed.

This study employs four systems of reference to formulate the equation of motion (EOM) of a vehicle as it moves along an arbitrary curved path (Fig. 3): an inertial (space-fixed) system *I*: *O-XYZ*, a moving trajectory system *TI*: O^{ti}-$X^{ti}Y^{ti}Z^{ti}$ [12], a body-fixed system *IR*: O^{ir}-$X^{ir}Y^{ir}Z^{ir}$ and a ground-fixed system *IG*: O^{G}-$X^{G}Y^{G}Z^{G}$ (Fig. 3), as in [11]. The motion of the *trajectory system* is pre-defined as the function of the arc length s^i (the

distance vehicle travels) along the central line of this track (Fig. 3). The longitudinal direction $O^{ti}X^{ti}$ is set tangent to the curve at the point O^{ti}.

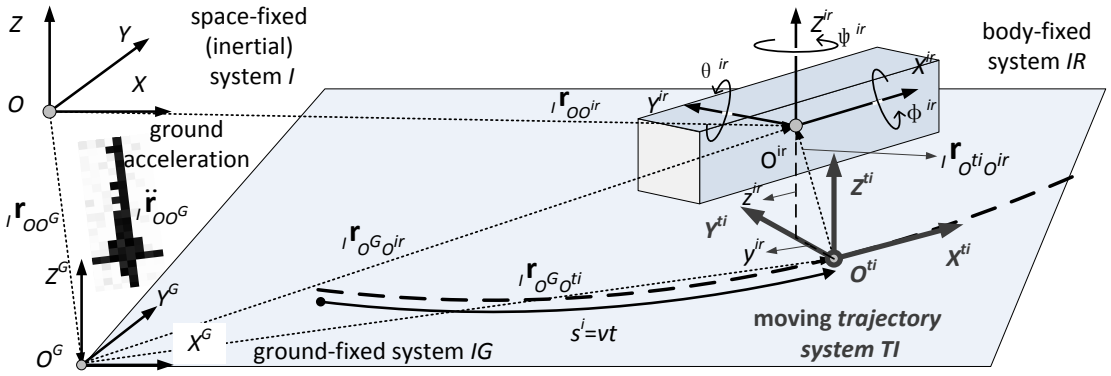

Fig. 3 – The four reference systems used in the presence of earthquakes: (i) space-fixed (inertial) system, (ii) moving trajectory system, (iii) body-fixed system and (iv) ground-fixed system.

The Newton-Euler EOM to describe the motion of the rigid body in terms of the generalized trajectory coordinates is [11]:

$$\mathbf{M}^i \ddot{\mathbf{p}}^i = \mathbf{F}_e^i + \mathbf{F}_v^i \tag{1}$$

where $\ddot{\mathbf{p}}^i$ is the generalized acceleration vector with six DOFs defined in terms the derivatives of the trajectory coordinates [11]:

$$\ddot{\mathbf{p}}^i = \begin{bmatrix} \ddot{s}^i & \ddot{y}^{ir} & \ddot{z}^{ir} & \ddot{\psi}^{ir} & \ddot{\phi}^{ir} & \ddot{\theta}^{ir} \end{bmatrix}^{\mathrm{T}} \tag{2}$$

and

$$\begin{cases} \mathbf{M}^i = m^i \mathbf{L}^{i^{\mathrm{T}}} \mathbf{L}^i + {}_{IR}\mathbf{H}^{i^{\mathrm{T}}}\, {}_{IR}\mathbf{I}^i_{\theta\theta}\, {}_{IR}\mathbf{H}^i \\ \mathbf{F}_e^i = \mathbf{F}_g^i + \mathbf{F}_G^i - \mathbf{F}_K^i - \mathbf{F}_C^i \\ \mathbf{F}_v^i = -m^i \mathbf{L}^{i^{\mathrm{T}}} \boldsymbol{\gamma}_R^i - {}_{IR}\mathbf{H}^{i^{\mathrm{T}}} \left({}_{IR}\mathbf{I}^i_{\theta\theta}\, {}_{IR}\boldsymbol{\gamma}^i_{\alpha} + {}_{IR}\boldsymbol{\Omega}^i \times \left({}_{IR}\mathbf{I}^i_{\theta\theta}\, {}_{IR}\boldsymbol{\Omega}^i \right) \right) \end{cases} \tag{3}$$

m^i is the mass of the rigid body; ${}_{IR}\mathbf{I}^i_{\theta\theta}$ is the inertia tensor defined in the body-fixed system about the principle axis. $\mathbf{F}_e^i$ is the external forces vector and $\mathbf{F}_v^i$ is the inertial forces vector (including the centrifugal forces and coriolis forces) that are quadratic in velocity. $\mathbf{F}_g^i$ is the gravity force vector; $\mathbf{F}_G^i$ is the seismic loads vector; $\mathbf{F}_K^i$ is the vector of the elastic forces in the suspensions; $\mathbf{F}_C^i$ is the vector of the damping forces. ${}_{IR}\boldsymbol{\Omega}^i$ is the angular velocity vector in the body-fixed system. $\mathbf{L}^i$ and ${}_{IR}\mathbf{H}^i$ are velocity transformation matrices. $\boldsymbol{\gamma}_R^i$ and $\boldsymbol{\gamma}_{\alpha}^i$ are

vectors containing the additional quadratic generalized velocity terms produced during the time-differentiation of the absolute translational velocity and the absolute angular velocity vector, accordingly.

Gathering the EOMs of each rigid body (i.e. the car body, bogies and wheelsets) together, and replacing the stiffness force vector and the damping force vector from Eq. (3) with their matrix expression, the EOM for the vehicle subsystem becomes:

$$\mathbf{M}^V(t)\ddot{\mathbf{u}}^V + \mathbf{C}^V\dot{\mathbf{u}}^V + \mathbf{K}^V\mathbf{u}^V - \mathbf{W}_N^V\boldsymbol{\lambda}_N - \mathbf{W}_T^V\boldsymbol{\lambda}_T = \mathbf{F}^V \tag{4}$$

where: $\mathbf{M}^V(t)$, $\mathbf{K}^V$ and $\mathbf{C}^V$ are the mass matrix, the stiffness matrix and the damping matrix of the vehicle system. $\mathbf{u}^V$, $\dot{\mathbf{u}}^V$ and $\ddot{\mathbf{u}}^V$ are the displacement, velocity and acceleration vector of the vehicle, accordingly. $\mathbf{F}^V$ is the force vector, including the gravity, the seismic and the centrifugal and the coriolis forces acting on the vehicle. $\mathbf{W}_N^V$ and $\mathbf{W}_T^V$ are the contact direction matrices of the vehicle correspond to $\boldsymbol{\lambda}_N$ and $\boldsymbol{\lambda}_T$ (to be discussed in Chapter 4).

3. Bridge modelling

The study models the bridge with the (3D) Euler-Bernoulli finite beam elements, utilizing linear and cubic (Hermitian) shape functions [11]. Each node has six DOFs: three displacements and three rotations with respect to the X, Y and Z axis accordingly. The EOM for the bridge system is:

$$\mathbf{M}^B\ddot{\mathbf{u}}^B + \mathbf{C}^B\dot{\mathbf{u}}^B + \mathbf{K}^B\mathbf{u}^B + \mathbf{W}_N^B\boldsymbol{\lambda}_N + \mathbf{W}_T^B\boldsymbol{\lambda}_T = \mathbf{F}^B \tag{5}$$

where $\mathbf{M}^B$ is the mass matrix and $\mathbf{K}^B$ is the stiffness matrix for the entire bridge. $\mathbf{C}^B$ is a Rayleigh damping matrix, calculated by assuming the damping ratio for the first two modes is 5%. $\mathbf{u}^B$ is the bridge displacement vector and $\mathbf{F}^B$ is the vector of the external loads, including the seismic forces. $\mathbf{W}_N^B$ and $\mathbf{W}_T^B$ are the contact direction matrices for the bridge subsystem, which contain the linear shape functions for the torsional DOFs and the cubic (Hermitian) shape functions for the flexural DOFs for beam elements.

4. Interaction modelling

The contact forces between wheels and rails couple the vehicle system and the bridge system. The EOM of the coupled vehicle-bridge system becomes:

$$\mathbf{M}^*(t)\ddot{\mathbf{u}} + \mathbf{C}\dot{\mathbf{u}} + \mathbf{K}\mathbf{u} - \mathbf{W}\boldsymbol{\lambda} = \mathbf{F} \tag{6}$$

where the global mass matrix $\mathbf{M}^*(t)$, the global stiffness matrix $\mathbf{K}$, the global damping matrix $\mathbf{C}$, the displacement vector $\mathbf{u}$, the external force vector $\mathbf{F}$, the contact force vector $\boldsymbol{\lambda}$ and the direction matrices $\mathbf{W}_N$ and $\mathbf{W}_T$ are created by gathering the pertinent matrices/vectors of the two individual subsystems as:

$$\begin{cases} \mathbf{M}^*(t)=\begin{bmatrix}\mathbf{M}^V(t) & \mathbf{0}\\ \mathbf{0} & \mathbf{M}^B\end{bmatrix},\ \mathbf{C}=\begin{bmatrix}\mathbf{C}^V & \mathbf{0}\\ \mathbf{0} & \mathbf{C}^B\end{bmatrix},\ \mathbf{K}=\begin{bmatrix}\mathbf{K}^V & \mathbf{0}\\ \mathbf{0} & \mathbf{K}^B\end{bmatrix}, \\ \mathbf{u}=\begin{bmatrix}\mathbf{u}^V\\ \mathbf{u}^B\end{bmatrix},\ \mathbf{F}(t)=\begin{bmatrix}\mathbf{F}^V(t)\\ \mathbf{F}^B\end{bmatrix},\ \boldsymbol{\lambda}=\begin{bmatrix}\boldsymbol{\lambda}_N\\ \boldsymbol{\lambda}_T\end{bmatrix}, \\ \mathbf{W}=\begin{bmatrix}\mathbf{W}_N & \mathbf{W}_T\end{bmatrix},\ \mathbf{W}_N=\begin{bmatrix}\mathbf{W}_N^V\\ -\mathbf{W}_N^B\end{bmatrix},\quad \mathbf{W}_T=\begin{bmatrix}\mathbf{W}_T^V\\ -\mathbf{W}_T^B\end{bmatrix} \end{cases} \tag{7}$$

$\boldsymbol{\lambda}$ is the contact force vector containing the normal contact force vector $\boldsymbol{\lambda}_N$, and the creep forces $\boldsymbol{\lambda}_T$ (the longitudinal creep force $\boldsymbol{\lambda}_{Tx}$, the lateral creep force $\boldsymbol{\lambda}_{Ty}$ and the spin moment $\boldsymbol{\lambda}_{Mz}$) due to the rolling contact (Fig. 4 (a)). The calculation of the creep forces is based on the Shen-Hedrick-Euristic model [11]. When the creepage (i.e. the normalized contact velocity) is small, the creep force follows a linear relation with the creepage (Fig. 4 (b)). For higher creepage conditions, e.g. during earthquakes, the relationship between the creepage and the creep force becomes nonlinear (Fig. 4 (b)). The normal continuous contact is calculated assuming zero contact acceleration at the interface, i.e. the kinematic constraint (Fig. 4 (c)) [13]. The contact-detachment transition of the wheel from the rail is captured as a Linear Complimentary Problem with zero normal contact forces - *a nonsmooth approach* (Fig. 4 (c)) [13]. The impact follows the Newton's law in the normal direction and the Coulomb's friction law in the tangential direction. The velocity jump associated with impacts is captured on the velocity level [13]. The wheel-rail impact occurs when the normal contact displacement g_N becomes zero with negative normal contact velocity $\dot{g}_N$ [13]. The coefficient of restitution is taken as $\varepsilon_N = 0$ [13].

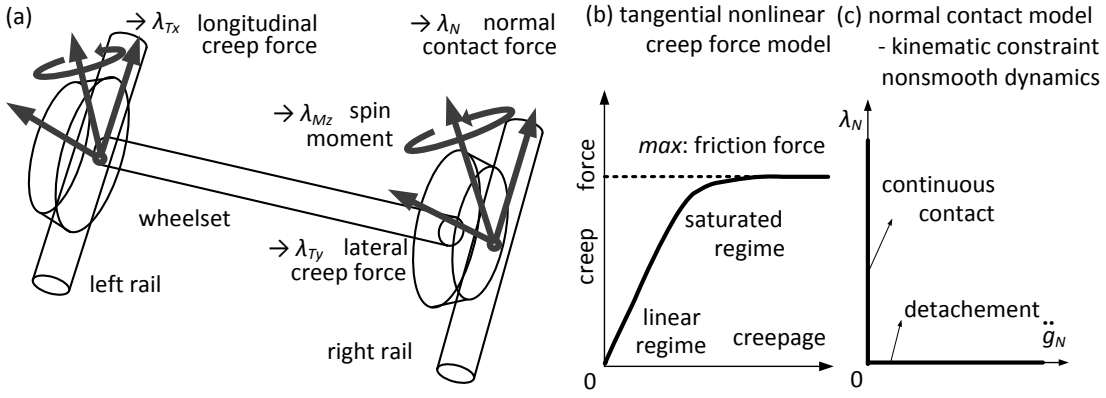

Fig. 4 – (a) Wheel-rail creep contact model, (b) tangential contact model, (c) normal contact model.

The profiles of the UIC 60 rail wheel surface and the S1002 wheel surface are discretized by a series of points with known coordinates (Fig. 5 (a)) [9]. Depending on the locus of the contact point, the contact is classified as thread contact or flange contact (Fig. 5 (b)). The normal and the tangential directions of contact, the contact angle and the rolling radius of each wheel (Fig. 5 (c)) are functions of the lateral wheel-rail displacement, and are all key parameters to the calculation of the contact forces.

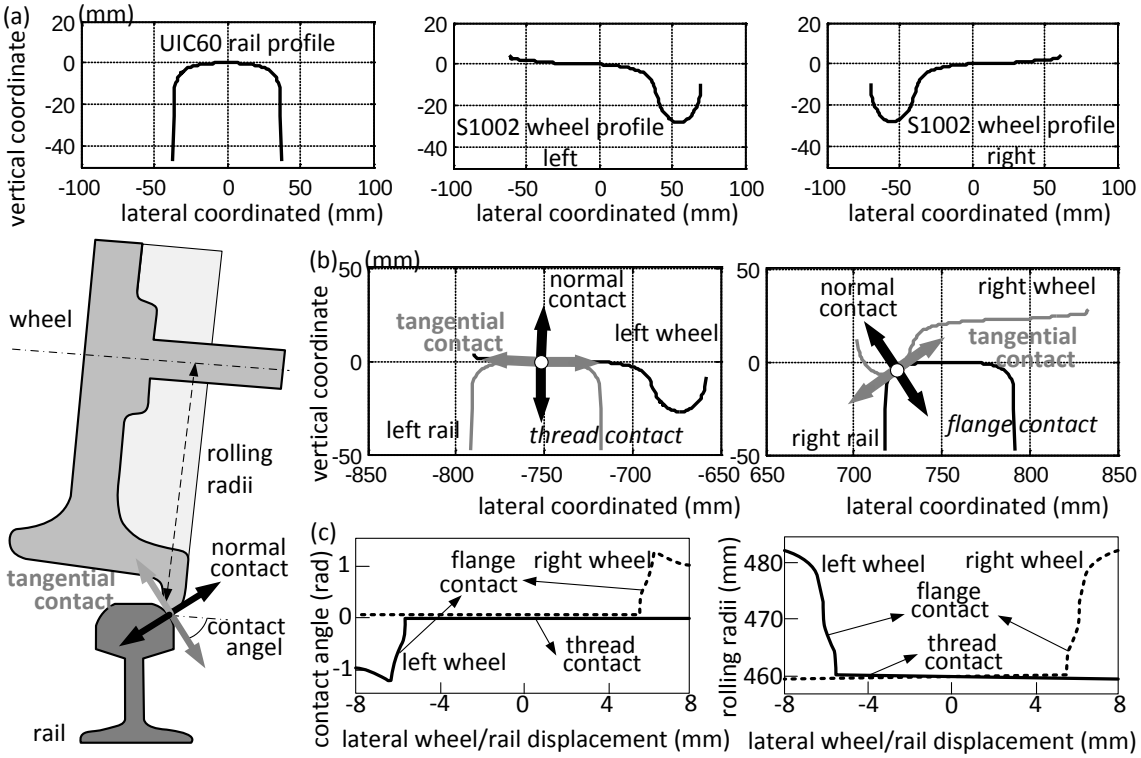

Fig. 5 – (a) The coordinates of the UIC 60 rail wheel and the S1002 wheel, (b) wheel-rail contact kinematics of thread and flange contact, (c) the contact angle and the rolling radii as the function of the lateral wheel-rail displacement.

Finally, the coupled EOM for the bridge-vehicle system is

$$\mathbf{M}^*(t)\ddot{\mathbf{u}}(t)+\mathbf{C}^*(t)\dot{\mathbf{u}}(t)+\mathbf{K}^*(t)\mathbf{u}(t)=\mathbf{F}^*(t) \tag{8}$$

with

$$\begin{cases}\mathbf{C}^*=\left[\mathbf{E}-\mathbf{W}(t)\mathbf{G}(t)^{-1}\mathbf{W}(t)^{\mathrm{T}}\mathbf{M}^*(t)^{-1}\right]\mathbf{C}+2v\mathbf{W}(t)\mathbf{G}(t)^{-1}\mathbf{W}'(t)^{\mathrm{T}}\\ \mathbf{K}^*=\left[\mathbf{E}-\mathbf{W}(t)\mathbf{G}(t)^{-1}\mathbf{W}(t)^{\mathrm{T}}\mathbf{M}^*(t)^{-1}\right]\mathbf{K}+v^2\mathbf{W}(t)\mathbf{G}(t)^{-1}\mathbf{W}''(t)^{\mathrm{T}}\\ \mathbf{F}^*=\left[\mathbf{E}-\mathbf{W}(t)\mathbf{G}(t)^{-1}\mathbf{W}(t)^{\mathrm{T}}\mathbf{M}^*(t)^{-1}\right]\mathbf{F}(t)-v^2\mathbf{W}(t)\mathbf{G}(t)^{-1}\mathbf{r}_c''\end{cases} \tag{9}$$

where $\mathbf{E}$ is an identity matrix and v the forward speed of the vehicle. The global mass matrix $\mathbf{M}^*(t)$ is time-dependent because of the curved path. The stiffness matrix $\mathbf{K}^*(t)$, the damping matrix $\mathbf{C}^*(t)$ and the loading vector $\mathbf{F}^*(t)$ become coupled and time-dependent, due to the interaction, reflecting the physical reality of the VBI phenomenon. The coupled and nonlinear EOM (9) is numerically integrated in a state-space form using the available ordinary differential equation (ODE) solvers for large, stiff systems.

5. Results and discussion

In the first example, consider a single train vehicle traveling along a horizontally curved track over the rigid embankment, during a strong earthquake. The speed of the vehicle is v = 300 km/h (83.33 m/s), and the radius of the curve is R = 10000 m. Fig. 6 plots the time histories of the strong ground motion recorded on 25 April, 1992 in Cape Mendocino USA, at Petrolia station during a 7.01 magnitude earthquake event [14]. The time duration of the earthquake ground motion is 36 s. The ground excitations act on the lateral (Y) and the vertical (Z) DOFs of all the components of the vehicle.

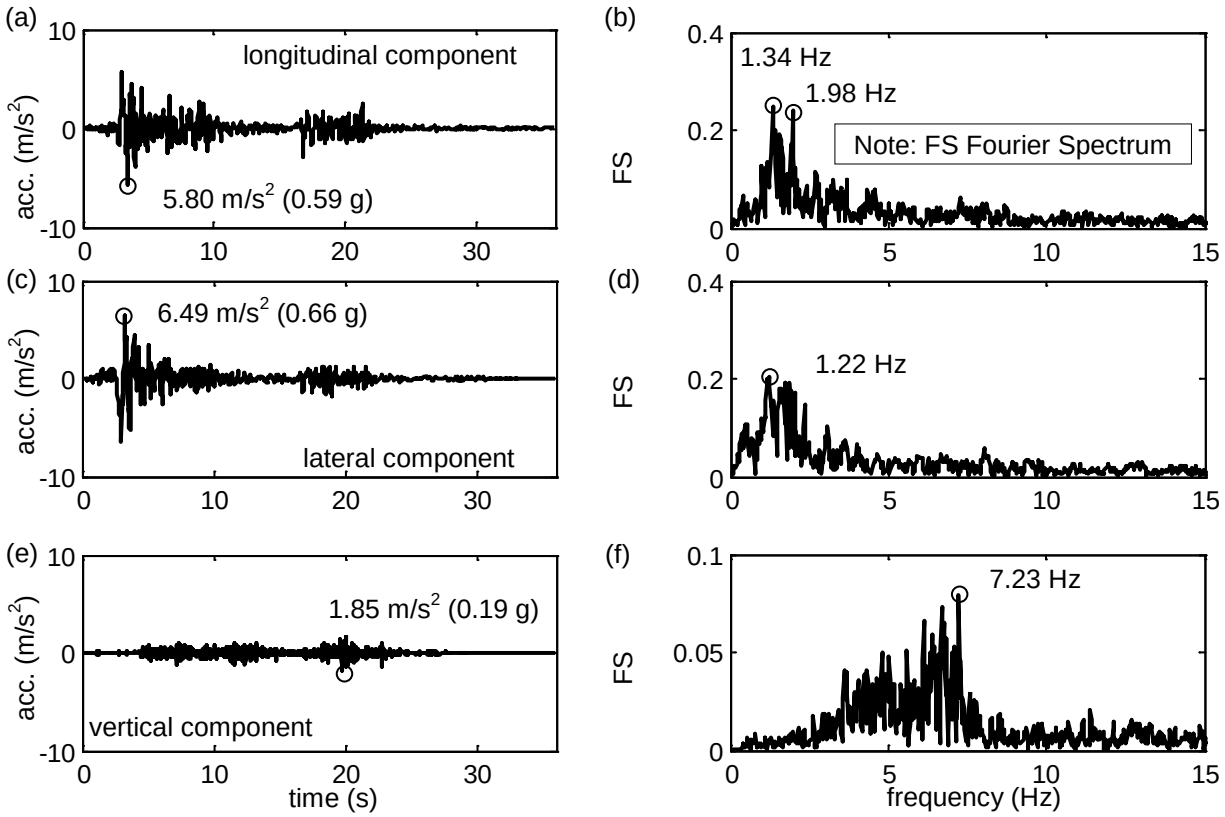

Fig. 6 –The acceleration time histories (a, c and e) and pertinent Fourier spectra (b, d and f) of the three components of the ground motion recorded on April 25, 1992 in Cape Mendocino USA, at Petrolia station.

Fig. 7 plots the response of the vehicle under the considered strong earthquake. Under the strong earthquake of Fig. 6, as expected, both the radial and the vertical peak accelerations exceed the "comfort" threshold of HSR codes of 0.98 m/s^2 (radial) and 1.28 m/s^2 (vertical) [15] (Figs. 7 (a) and (b)). Figs. 7 (c) and (d) plots the radial and the rolling car body displacement time histories. The car body vibrates due to the earthquake. Figs. 7 (e) and (f) plot the normal contact force of wheel 1 and the pertinent zoom-in. The detachment happens at t = 15.402 s and t = 15.455 s, with the pertinent value of the normal contact force becomes zero. After the impact and recontact, the normal contact force becomes non-zero at the time instant of t = 15.430 s and t = 15.466 s. The peak *derailment factor* and the *offload factor* are close to the corresponding

thresholds of 0.8 and 0.6 (Figs. 7 (g) and (h)), which are important metrics to evaluate the running safety of the vehicle in the code [15].

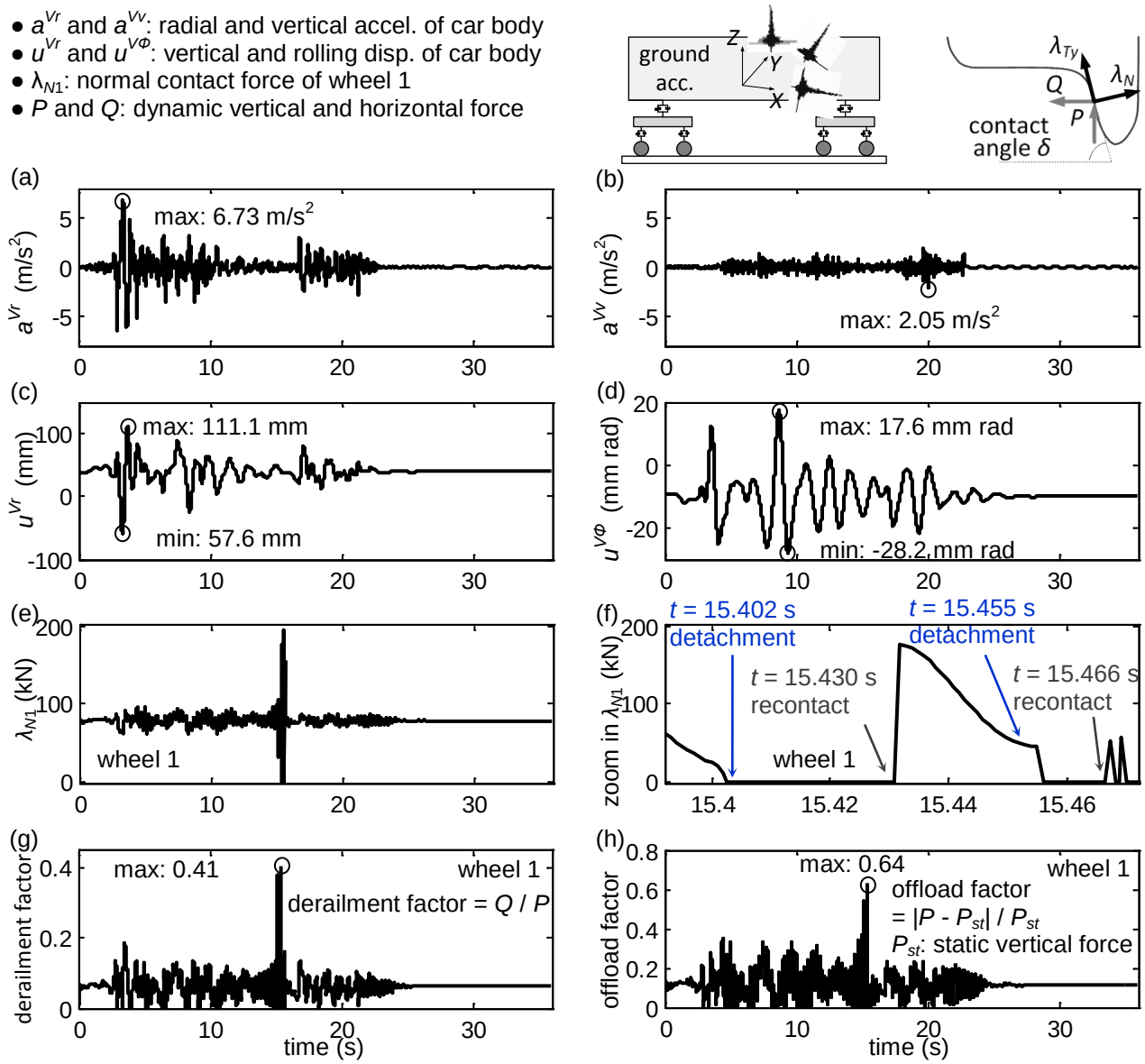

Fig. 7 – The response of the vehicle under the strong earthquake: the (a) radial and the (b) vertical car body acceleration time histories, the (c) radial and the (d) rolling car body displacement time histories, the (e) normal contact force time histories and (f) the pertinent zoom-in of wheel 1, the (g) derailment and the (h) offload factor time histories of wheel 1.

Fig. 8 plots the contact kinematics of the wheel and the rail for the first wheelset (wheels 1 and 2) under the earthquake of Fig. 6. Originally (t = 0 s) both wheels 1 and 2 are in thread contact with the rail at the stationary state. Wheel 1 detaches from the rail at t = 15.402 s; simultaneously, wheel 2 is in flange contact (Fig. 8 (b) right). Further, Fig. 8 (c) left captures the state of the uplifting of wheel 1 at t = 15.428 s (between t =

15.402 s and t = 15.430 s). The wheel 1 gets recontact with the rail at t = 15.430 s with a the zero normal contact distance between the wheel and the rail (Fig. 8 (d) left).

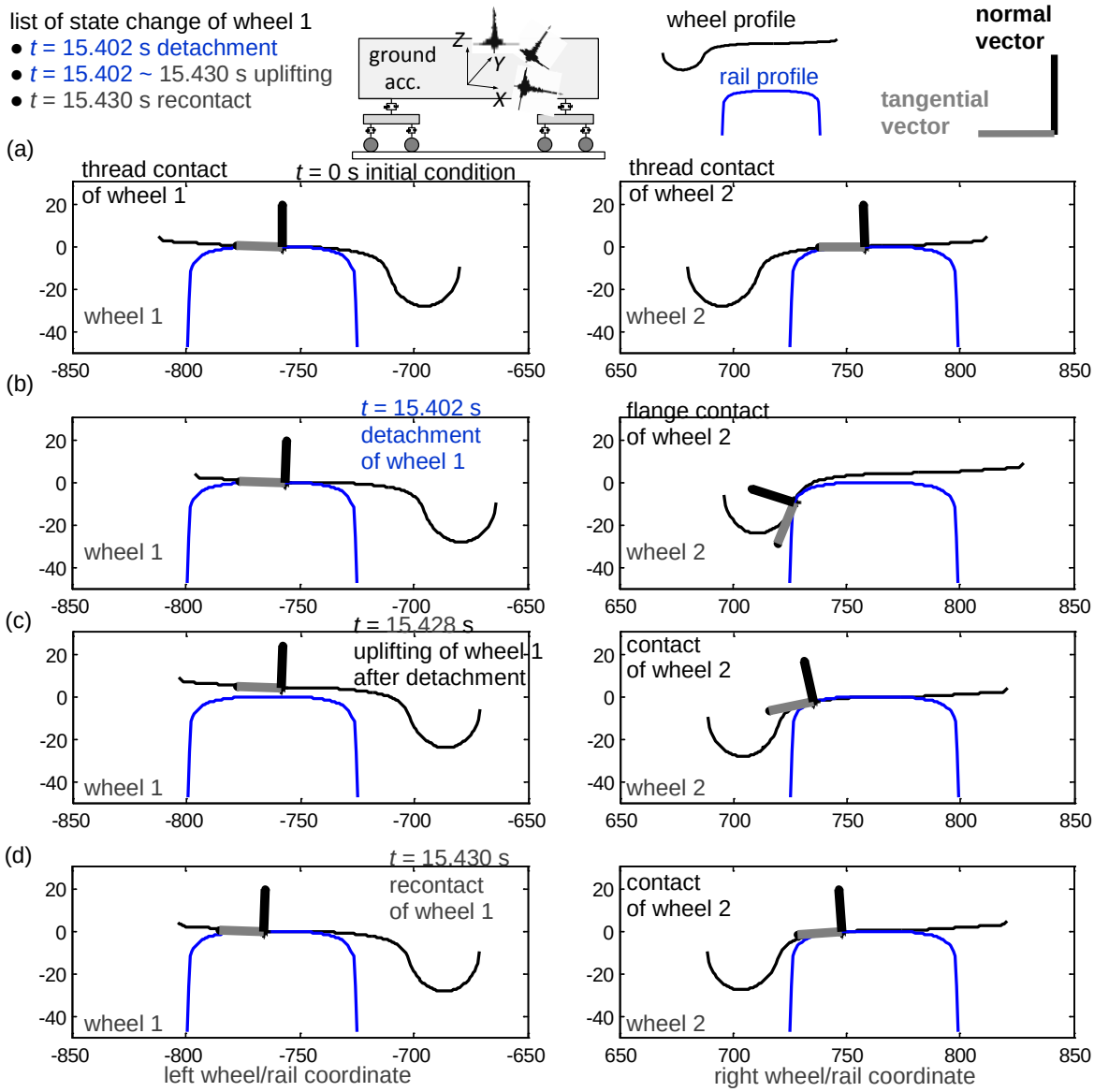

Fig. 8 – The wheel-rail kinematics for wheelset 1 (wheels 1 and 2) for four different wheel-rail contact states: (a) initial condition, (b) the state before the detachment of wheel 1, (c) the state after the detachment of wheel 1 and (d) the impact and recontact of wheel 1.

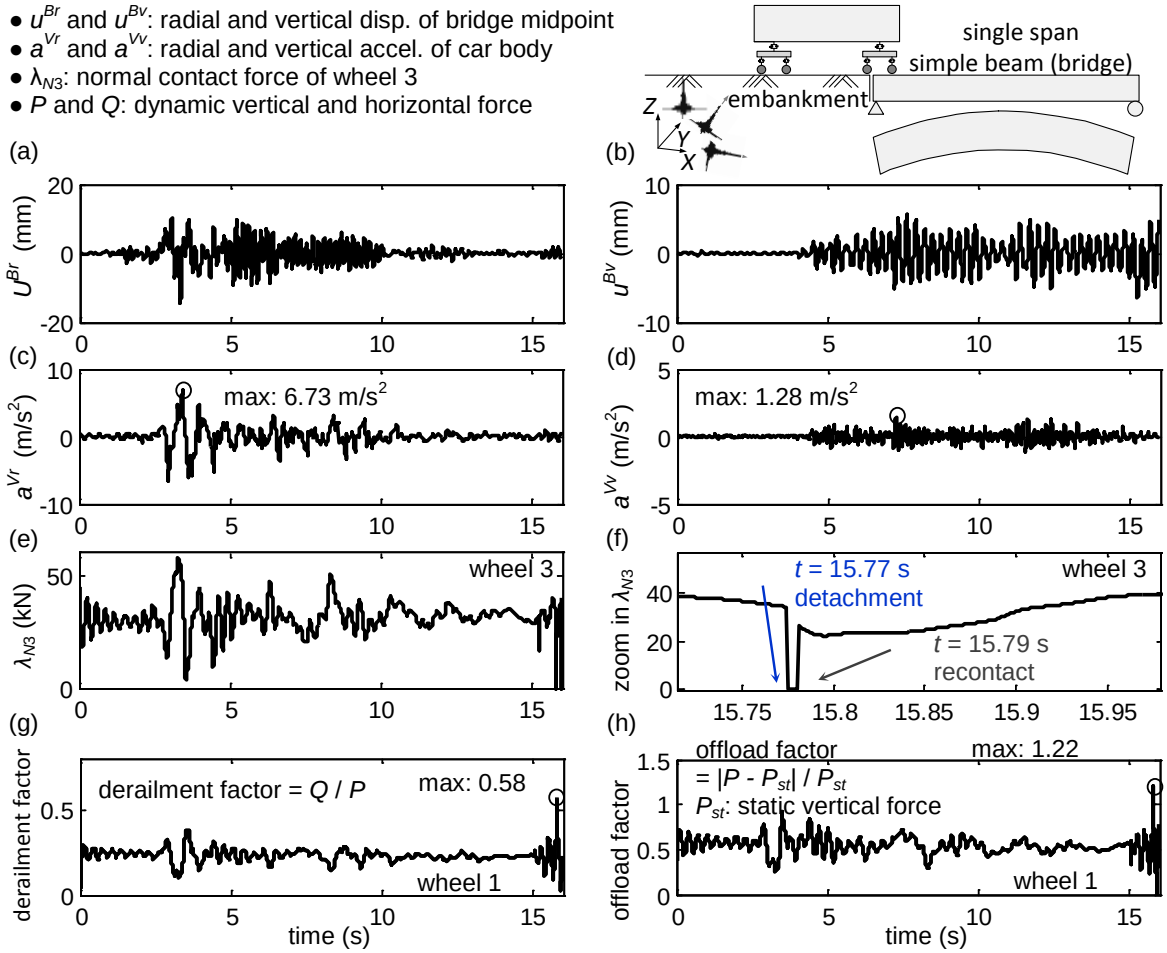

Fig. 9 – The response of the bridge and the vehicle under the strong earthquake of Fig. 6: the (a) radial and the (b) vertical displacement time histories of the bridge midpoint, the (c) radial and the (d) vertical car body acceleration time histories, the (e) normal contact force time histories and (f) the pertinent zoom-in of wheel 3, the (g) derailment and the (h) offload factor time histories of wheel 1.

The second example exams the same vehicle travelling along a single span horizontally curved simply supported bridge (Fig. 9 top right), with the properties given in [1], during the same strong earthquake of Fig. 6. The length of the bridge is 32 m. From Fig. 7, the detachment occurs after around 15.4 s, when the vehicle travels over the embankment under the considered earthquake. The earthquake excitation starts at t = 0 s and the vehicle enters the bridge after 15.3 s travelling over the embankment. The vehicle leaves the bridge at 16 s, after which, the response of the VBI system is of on interest (Fig. 9). Fig. 9 plots the response of the bridge and the vehicle, under the strong earthquake. The vibration of the bridge is controlled by the earthquake rather than the moving vehicle (Fig. 9 (a) and (b)). The detachment of wheel 3 happens at the time 15.77 s with zero normal contact force. Specially, the *derailment factor* and the *offload factor* of the wheel 1 on the embankment (Figs. 7 (g) and (h)) is smaller than the values on the bridge (Figs. 9 (g) and (h)), indicating the adverse effect of the seismic induced vibration of the bridge on the response of the vehicle. Recall [11], that the position of the

running vehicle on the deck, during the strong earthquake shaking, is an inherently stochastic problem which beckons for probabilistic treatment. However, this task is beyond the scope of this study.

6. Conclusions

The study examines the seismic behavior of a coupled train-bridge system under strong earthquakes. The proposed contact model can capture the flange contact, the detachment, the uplifting and the recontact phenomena between the wheel and the rail. In the cases examined, the detachment of a wheel happens when the other wheel belonging to the same wheelset is in flange contact. After the detachment, the pertinent normal contact force becomes zero and the wheel jumps from the rail. The wheel re-contacts with the rail when the normal contact distance becomes zero. The results show that the seismic induced vibration of the bridge has a significant adverse effect on the response of the train. Given the recent developments on high-speed railways, worldwide and especially in Asia, this is an issue of increasing importance which merits further study.

7. References

[1] Zeng Q, Yang YB, Dimitrakopoulos EG (2016): Dynamic response of high speed vehicles and sustaining curved bridges under conditions of resonance. Engineering Structures, 114, 61-74.

[2] Ashford SA, Kawamata Y (2006): Performance of transportation systems during the 2004 Niigata Ken Chuetsu, Japan, earthquake. Earthquake Spectra, 22, 111-132.

[3] Kao TC (2011): Lecture note: High speed rail engineering.

[4] Ogura M (2006): The Niigata Chuetsu Earthquake-railway response and reconstruction. Japan Railway & Transport Review, 43, 46-63.

[5] Yang YB, Wu YS (2002): Dynamic stability of trains moving over bridges shaken by earthquakes. Journal of Sound and Vibration, 258, 65-94.

[6] Tanabe M, Wakui H, Sogabe M, Matsumoto N, Tanabe Y (2011): An efficient numerical model for dynamic interaction of high speed train and railway structure including post-derailment during an earthquake. 8th International Conference on Structural Dynamics, EURODYN, Leuven, Belgium, 1217-1223.

[7] Ju SH (2012): Nonlinear analysis of high-speed trains moving on bridges during earthquakes. Nonlinear Dynamics, 69, 173-183.

[8] Du XT, Xu YL, Xia H (2012): Dynamic interaction of bridge-train system under non-uniform seismic ground motion. Earthquake Engineering & Structural Dynamics, 41, 139-157.

[9] Montenegro PA, Neves SGM, Calçada R, Tanabe M, Sogabe M (2015): Wheel-rail contact formulation for analyzing the lateral train-structure dynamic interaction. Computers & Structures, 152, 200-214.

[10] Dimitrakopoulos EG, Zeng Q (2015): A three-dimensional dynamic analysis scheme for the interaction between trains and curved railway bridges. Computers & Structures, 149, 43-60.

[11] Zeng Q, Dimitrakopoulos EG (2016): Seismic response analysis of an interacting curved bridge-train system under frequent earthquakes. Earthquake Engineering & Structural Dynamics, 45, 1129-1148.

[12] Shabana AA, Zaazaa KE, Sugiyama H (2010): Railroad Vehicle Dynamics: A Computational Approach. CRC Press, New York.

[13] Pfeiffer F, Glocker C (1996): Multibody Dynamics with Unilateral Contacts. John Wiley and Sons, Singapore.

[14] http://ngawest2.berkeley.edu/site (Accessed 05/04 2015).

[15] China's Ministry of Railways (2009): Code for Design of High Speed Railway.